MULTI-PHENOMENOLOGY OBSERVATION NETWORK EVALUATION TOOL (MONET)

Daniel L. Oltrogge
Sr. Research Astrodynamicist, Center for Space Stds. and Innovation, Analytical Graphics Inc.
Patrick North
Sr. Software Engineer, Analytical Graphics Inc.
Michael Nicolls
Program Manager / Staff Scientist, Center for Geospace Studies, SRI International

1.   Abstract

Evaluating overall performance of a ground- and/or space-based SSA "system-of-systems" observational network collecting against thousands of Resident Space Objects (RSO) is very difficult for typical tasking or scheduling-based analysis tools. This is further complicated by networks that have a wide variety of sensor types and phenomena (e.g., optical, radar and passive RF types), each having unique performance, resources, ops tempo, and competing customer and detectability constraints.

We present details of the "Multi-phenomenology Observation Network Evaluation Tool" (MONET), which circumvents these difficulties by assessing the ideal performance of such a network via a digitized supply-vs-demand approach. Cells of each sensor's supply time are distributed among RSO targets of interest to determine the average performance of the network against that set of RSO targets. Orbit Determination (OD) heuristics are invoked to represent observation quantity and geometry notionally required to obtain the desired orbit estimation quality.

To feed this approach, we derive the detectability and collection rate performance of optical, radar and passive RF sensor physical and performance characteristics. We then prioritize the selected RSO targets according to object size, active/inactive status, orbit regime, and/or other necessary considerations. Finally, the OD-derived tracking demands of each RSO of interest are levied against remaining sensor supply until either (a) all sensor time is exhausted, or (b) the list of RSO targets is exhausted. The outputs from MONET include overall network performance metrics delineated by sensor type and objects and orbits tracked, along with likely orbit accuracies corresponding to the conglomerate network tracking predicted performance.

2.   MONET System-Of-Systems Performance Evaluation via Digitization

System performance characterization and optimization are especially vital for space object tracking network observations of Resident Space Objects (RSOs). Such characterization and optimization are complicated by the embedded tracking geometries, sensor performance evaluation, sensor resource management, optimal scheduling, and sensor assignment aspects of the problem.

In prior work, Dan Oltrogge conceived, designed and developed algorithms and software for an Earth observations system-of-systems analysis and performance evaluation program called BLINE (pronounced Bee-Line). BLINE is a unique time-varying evaluation of satellite supply versus ground "target" demand, which works by digitizing (i.e., breaking up both observing satellite resource supply and ground target demand into "tiny bits," and optimally divvying demand bits to the satellites' "supply bits." BLINE is an improved version of an older, time-invariant analysis tool called BSPACE[1], which the author also contributed to and developed.

As previously noted[1], conclusions from independent validations of such a supply-versus-demand digitization approach were that "The accuracy of the simulation has been tested and found to be within approximately 5% of that of a traditional deterministic simulator" and "[The digitization approach] produces results comparable to the best of the medium- to high-fidelity simulations currently in use. A statistical sampling approach allows excellent results to be obtained with far fewer computational steps than are required by an equivalent deterministic algorithm."

To illustrate how such digitization works, let's assume a single ground target that we want to observe which is observable by three satellites over a given period of time during which we want to observe the ground target. In the digitized world, ground target if observed (if possible), but satellite time and resources needed to observe the target are divvied up such that each of the three satellites spends some of its resources to observe "a part" of the ground target. The amount of time and resources divvied to each of the three satellites depends on their respective collection rates, remaining supply, and other weighting factors (including sensor degradation due to cloud cover). In stark contrast, the reality is that only one of the satellites is tasked to observe the target, and the other two satellites would be idle (for that target). So, for this single target, we can see that we've improperly (but proportionately) assigned the target's demand to three satellites when only one is actually tasked.

Yet, when allocating observing sensor resources to a target deck consisting of many thousands of ground, independent testing confirms that breaking target demand into digitized parts properly reflects not only the resources each satellite spends and how many targets are collected, but it also presents an idealized optimal divvying of ground targets to system-of-systems constellation(s) to which the best scheduling algorithms can aspire.

We realized that this same approach to optimally divvying digitized sensor supply to target observational demand could be applied to ground sensors looking up at targets in space, as were those successfully applied to space sensors looking down. Just as the impressionist artist Claude Monet used "digitized" dots of paint that the eye can aggregate to see the "big picture," we've developed MONET as the digitized implementation of ground or space observers against the hundreds of thousands of Resident Space Objects (estimated to be over 700,000 RSOs down to a size of 1 cm) which need to be tracked for mature Space Situational Awareness (SSA).

3.   Optimal Demand Allocation Using the Digital Paradigm

For MONET, we adopted a similar approach to optimal digital allocation of sensor supply as was used in the aforementioned ground-observing tools. As previously noted[1], "The Valley-Fill algorithm, invented by Dan Oltrogge, balances imaging supply and demand. The algorithm was developed to push the need for imaging time closer to the opportunities to receive it, and to distribute available resources such that all targets are supplied with the most imaging time available to them." If desired, digitized network bandwidth & buffers can also be simulated.

As implemented in MONET, the steps to optimally allocate digitized supply are as follows:

(1) The input RSO list is sorted such that the highest-priority RSOs are processed first;
(2) The positions and lighting conditions for all active observing sensors are propagated at a fine mesh size (e.g. 1 second) for the full analysis timespan (e.g. 1 year) and stored;
(3) The "supply time" for each sensor is initialized to the amount of time each mesh grid point represents;
(4) Each "i^{th}" RSO:
   a. The ith RSO is initialized and positionally propagated;
   b. The full analysis timespan is stepped through in increments of the periodicity of the target demand. For example, if the goal is to track an RSO three times per orbit, then the mesh grid is evaluated in sub-meshes that are (orbit period/3) in duration.
   c. Within each sub-mesh grid point/time, sensor visibilities and (when visible) sensor collection rates are computed;
   d. Target demand is allocated to all cells having legitimate target visibility (denoted with subscript "i") within the sub-mesh timespan using the following sequence of steps:
      i.   Accumulate their remaining supply time (Figure **1**) for all cells that <u>could</u> successfully collect against all or some portion of the target's demand;
      ii. Sort the cells by their individual remaining supply time (Figure **2**);
      iii. Attempt to put all of the target's demand into cell #1 (with greatest remaining supply) as shown in Figure **3**.
      iv. Progressively shift the target demand to subsequent neighboring cells until the remaining supply time in the utilized cells is higher than the supply time of the next adjacent neighboring cell of the sorted descending list (Figure **4**).

   e. The relevant equations can be derived as follows:
      i.   Assume that every "i^{th}" cell's Existing Demand Time (EDT) is accumulated as:

Equation 1:
$$EDT_i = \sum_{j=1}^{\#old\ targets} D_{j_{old}} W_{j_{old}} R_{j_{old}}$$

where $D_{j_{old}}$, $W_{j_{old}}$ and $R_{j_{old}}$ denote the demand, additional demand weighting(s) (e.g., inflation due to cloudiness) and past collection rates for all portions of target demand that this cell has accommodated so far;

ii. Let "K" denote the constant supply time remaining, in common across all <u>utilized</u> cells having legitimate visibility, after accommodating the latest target's demand. Let the Existing (remaining) Supply Time (EST) of each "i^{th}" cell be denoted as EST_i (note that EST_i is by definition non-negative), such that for any given supply cell,

Equation 2:
$$K = EST_i - D_i\ W_i\ R_i = \text{a constant value for all utilized supply cells}$$

where D_i, W_i and R_i denote the demand, additional demand weighting(s) and collection rates for the new target;

iii. Solving for the accommodated portion of the target's demand D_i, we obtain:

Equation 3:
$$D_i = \frac{EST_i - K}{R_i W_i}$$

iv. The total demand accommodated for this single target is then:

Equation 4:
$$D_T = \left[\sum_{j=1}^{\#cells\ used} D_j\right] = \left(\frac{EST_1}{R_1 W_1} + \frac{EST_2}{R_2 W_2} + \frac{EST_3}{R_3 W_3} + \cdots\right) + \left(\frac{K}{R_1 W_1} + \frac{K}{R_2 W_2} + \frac{K}{R_3 W_3} + \cdots\right)$$

v. From which we can now solve for "K" assuming $D_T = Target's full\ demand$:

Equation 5:
$$K = \left[\sum_{i=1}^{\#cells} \frac{EST_i}{R_i W_i} - D_T\right] \Big/ \left[\sum_{i=1}^{\#cells} \frac{1}{R_i W_i}\right]$$

vi. Continue to shift demand to the next-adjacent-cell until either (a) K is less than the neighboring cell's remaining supply (in which case $D_T = Target's full\ demand$) or (b) all cells with legitimate visibility have been exhausted (in which case if K is less than zero, accommodated demand $D_T = \left[\sum_{j=1}^{\#cells\ used} D_j = \sum_{i=1}^{\#cells} \frac{EST_i}{R_i W_i}\right]$).
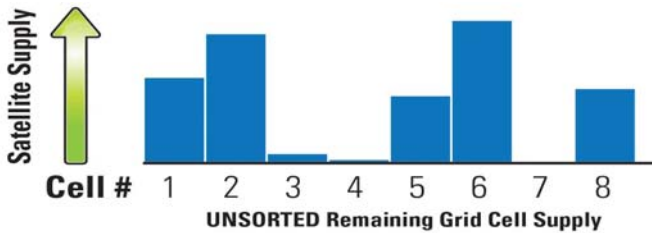

Figure 1. Sensor cells with visibility, unsorted by remaining grid supply time

Figure 2. Sensor cells with visibility, sorted by remaining grid supply time

Figure 3. Attempted (and failed) allocation of all of the current target's demand to sensor cell #
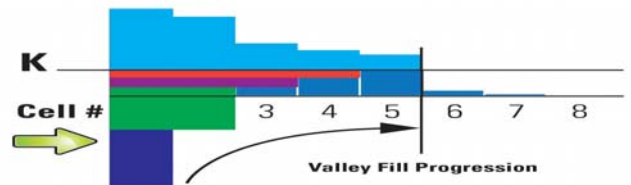

Figure 4. Ideal allocation of target demand, spread amongst all cells with visibility until the next-adjacent-neighbor has less supply than "K"

4. Embedded/Implied Tracking Prioritization Scheme

As presented above, note that the first targets accommodated by the sensor supply grid are most likely to be successfully tracked since the supply grid is "full" and untapped at the start of the analysis run. As a result, the target deck (e.g. RSO catalog) should best be sorted such that those RSOs of greatest importance to the analyst are processed first. For example, the analyst may wish to track active satellites first and spend remaining supply on tracking orbital debris. Alternately, the analyst may want to try to track the smaller objects and debris first.

In this paper, we sorted our RSO catalog "input target deck" such that the active satellites were addressed first (monotonically increasing from smallest to largest size), followed by the non-active RSOs (smallest to largest).

5. Assessing Tracking Needs as a Function of Desired Orbital Accuracy

Ultimately, the goal of any space tracking network is to maintain flawless positional knowledge and awareness of all objects in space. For tiny objects that are too small to track with existing technologies, this goal cannot be reached because the network's sensors are unable to detect and maintain custody of them.

The "Flawless positional knowledge" goal is also unachievable for a host of reasons, many of which are outside the sensor network's direct control (i.e. maneuvering objects, non-cooperative tracking that can introduce cross-tags and track misassociations, imperfect atmosphere models, space weather unpredictability, and lack of all-sky persistent coverage, and limited sensor tracking resources).

This last issue of sensor tracks being a finite (and typically constrained) resource is an important one, both in the real world and in MONET modeling. For MONET, the user is free to choose any method s/he desires to specify how much "demand" (i.e. how many tracks per orbit and how many observations per track) a given target needs to maintain desired orbit determination accuracy.

A recent AGI-internal empirical study examined the relationship between resultant orbit solution accuracy and the frequency of radar observational tracks (resources) allocated to a given space object in LEO. The study sought to minimize the positional error of tracked satellites while simultaneously minimizing the cost of a tracking system. AGI engineers were able to employ AGI's Components and STK Server technology to run Orbit Determination Tool Kit (ODTK) on 384 computational cores to parametrically analyze orbit determination performance on a wide variety of site locations, trackers per site, and satellites tracked over time. These combinations resulted in approximately 300,000 total filter runs which were efficiently analyzed as spread over the 384 cores.

For the purposes of the MONET implementation, one of the interesting "heuristics" found from this computationally-intensive and extensive study was that for observing sites having reasonable geographical diversity, an optimal performance combination of accuracy versus cost was achieved and an average maximum (i.e. around the entire orbit arc) post-orbit determination position error of 50 meters was met using a white noise sigma of 20 m, 10 observations per track and approximately 0.35 tracks per orbit.

For our MONET example test case, we will adopt this admittedly simple heuristic approach to govern how many times we will try to track each space object, while recognizing that much more sophisticated relationships and heuristics can be accommodated by the MONET digitization paradigm.

6. MONET Sensor Collection Performance and Rate Modeling

This "digital" method depends heavily upon the anticipated sensor performance and collection rates at each time point along the sensor location grid in inertial space. Details of our sensor capability and collection rate analytical formulations are now shared.

6.1 Ground-Based and Space-Based Optical Sensor Modeling In MONET

The purpose of the optical sensor modeling performance prediction is to be able to quickly and accurately assess the capability of a sensor to detect a given target under specific geometric, illumination, and local atmospheric conditions. In order to meet the speed requirements, an analytical method was developed and validated against more accurate, but also much more time consuming, empirical simulations. This allows for massive simulations and architecture trade studies to be performed with modest computing hardware capabilities.

In order to characterize the optical performance of sensors and targets under the conditions of interest, the environmental effects analyzed were illumination, relative geometry, and atmosphere. The solar illumination included the potential partial or complete shadowing from the earth of the satellite target. The relative geometry was characterized as the angle from the sensor to the sun relative to the target (also called the phase angle or the Critical Angle from Target to Sun or CATS). Finally, the atmospheric transmission loss from the target to the sensor, as well as the ambient path radiance or background illumination at the time of imaging, and the atmospheric distortion of the target, were modeled. These environmental effects can be seen graphically displayed below in Figure **5**. This setup provides accurate entrance aperture radiance for both the target and the background from the perspective of the sensor.
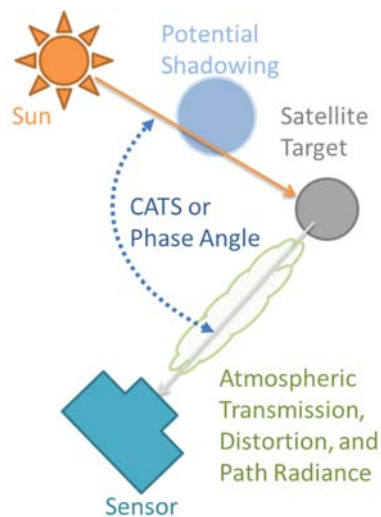

Figure 5. Environmental effects impacting optical performance

The defined concept of operations or ConOps for MONET is detecting predominantly small targets and thus the angular size of the targets will typically be smaller than the resolving power of the optical sensors, and therefore the targets can be treated as point sources. This is significant in that the analytical sensitivity equations are greatly simplified. For more perspective, the validity of this assumption can be characterized by comparing the angular subtense of target to the resolving power of the system. When the angular subtense converted into pixel space is much smaller than the *System-Q*, defined in Equation 6, then a point source approximation is appropriate and this analytical method is valid. If this assumption is not true, then a more involved but more accurate empirical simulation should be performed. The *System-Q* is a function of the wavelength of light being evaluated (λ, typically the mean sensor response in units of meters), the *F/#* of the optical sensor system (focal length divided by the clear aperture diameter of the sensor), and the detector spacing or pitch (p in units of meters) on the focal plane. The equations provided in this section with describe the full empirical modeling method and the analytical

approximation.   Finally, validation performed through simulation will be presented to assess the accuracy of this analytical approach.

Equation 6:
$$System - Q = \frac{\lambda\,F/\#}{p}\ \text{[pixels]}$$

The model used for calculating the reflected intensity of the target in the direction of the sensor (I_{Target}, **Error! Reference source not found.**) is a Lambertian gray sphere characterized by an in-band reflectance (ρ, *a unitless ratio*) and a cross-sectional area (A_{Target} in units of m^2). All of the quantities presented here are band–effective, spectrally-integrated values as another simplification. The impact of this simplification was found to be minimal for the optical sensors, targets, and environments being evaluated. However, a more accurate spectral representation could be used for greater fidelity or for more exotic scenarios that would require high resolution spectral modeling.

Equation 7:
$$I_{Target} = \frac{E_{Sun}\,F\,\rho\,Phase(\varphi)\,A_{Target}}{\pi}\ \text{[W/sr]}$$

The phase function (*Phase*) of a Lambertian is dependent only upon the phase angle (φ in radians) and characterized by Equation 3 which makes it an attractive and simple model. A constant exoatmospheric solar irradiance (E_{Sun} in units of W/m^2) was used to simplify the analysis; however a seasonally varying and geometrically accurate value could be used to increase fidelity. Also a general shadowing term (F, a unitless ratio) was derived and applied rather than explicitly integrating the penumbra regions influence.

Equation 8:
$$Phase(\varphi) = \frac{sin\,\varphi + (\pi - \varphi)\,cos\,\varphi}{\pi}\ \text{[ratio]}$$

The atmospheric transmission ($\tau_{Atmosphere}$, a unitless ratio) and background illumination or path radiance (L_{Path} in units of W/m^2 sr) are similarly treated as in-band quantities, and the values were calculated by using a Natural Sky Factor (*NSF*) term that is generally available by date and time over many geographic regions to characterize background illumination and also generating representative model atmospheres using MODTRAN 5.1 for specific transmission and path radiance values at various target zenith angles. The atmospheric turbulence distortion is modeled as a point-spread-function characterized by the optical seeing disc diameter ($d_{SeeingDisc}$, an angular dimension in units of radians). The optical seeing disc is another generally available astronomy parameter that can be estimated for the set of representative atmospheres used in this analysis. The target specific entrance aperture radiance ($E_{EntranceAperture}$) is given in Equation 9 and the atmospheric distortion and background illumination will considered later on in this section.

Equation 9:
$$E_{EntranceAperture} = \tau_{Atmosphere}(\theta)\,\frac{I_{Target}}{d_{TargetToSensor}^2}\ \text{[W/m}^2\text{]}$$

To this point all of the analysis has been sensor agnostic and this is a natural breakpoint to separate the environmental effects from the sensor effects. The next step is to take into consideration the sensor effects including the relative target motion, optical projection onto the focal plane, the conversion of focal plane irradiance to a digital signal, and finally the digital signal target detection performance. These steps can be visualized as in Figure 6.
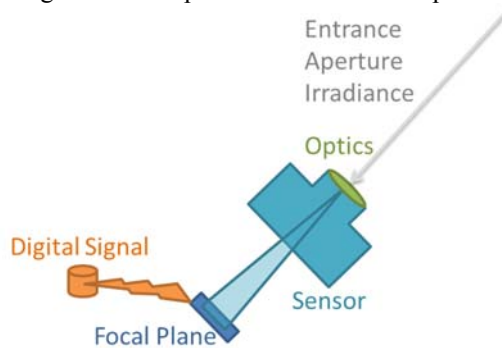

Figure 6. Sensor effects impacting optical performance

For point source targets, the entrance aperture irradiance is projected into focal plane flux ($\Phi_{FocalPlane}$) by the optics described in Equation 10, a function of the effective area of the optics or pupil function ($A_{Aperture}$ in units of m^2) and the effective optical transmission (τ_{Optics} as a unitless ratio) including any loss due to imperfect reflection, transmission, or obscuration of optical components. This flux is then converted into an analog target signal at a specific point (S_{Point}) by the detectors described in Equation 11, as a function of the integration time (t in units of s), the relative spectral response function (SRF as a band effective scaling ratio), quantum efficiency (QE in units of electrons/photon), and the energy per photon of the designated wavelength (Q_λ in units of joules/photon). These two equations, presented below, comprise the total system response of the sensor for the target signal.

Equation 10:
$$\Phi_{FocalPlane} = E_{EntranceAperture}\, A_{Aperture}\, \tau_{Optics} \text{ [W]}$$

Equation 11:
$$S_{Point} = \Phi_{FocalPlane} \frac{t\, SRF\, QE}{Q_\lambda} \text{ [Electrons]}$$

At this point we reintroduce the background illumination (L_{Path}) as a radiance that is projected onto the focal plane as irradiance and integrated over the detector area to form the background flux ($\Phi_{Background}$) defined in Equation 12. This flux can be converted to electrons just at the target flux was; however, at this point, the dark current ($n_{DarkCurrent}$) and read noise (n_{Read}) should be taken into consideration to get a more complete background signal level (B, Equation 13).

Equation 12:
$$\Phi_{Background} = L_{Path}(NSF) \frac{\tau_{Optics}\, \pi}{1+4\, F/\#^2}\, p^2 \text{ [W]}$$

Equation 13:
$$B = \Phi_{Background} \frac{t\, SRF\, QE}{Q_\lambda} + n_{DarkCurrent}t + n_{Read} \text{ [Electrons]}$$

All of the signal modeling to this point has been for point sources. However once the signal is recorded even the geometrically legitimate point source treatment will undergo spatial modulation due to the atmosphere, relative motion, optics, and detectors. These four sources of spatial transformations can be applied to the target point signal by modeling the entire system as a linear shift-invariant system. This can be done by treating the target signal as a delta function and convolving by the Point Spread Functions (PSF) of the atmosphere, relative motion, optics, and detectors. This is shown below in Equation 14, with the following PSF effects:

- Atmospheric PSF ($PSF_{Atmosphere}$) characterized by the seeing-disc diameter ($d_{SeeingDisc}$)
- Relative motion blur PSF ($PSF_{MotionBlur}$) is characterized by the smear rate (v_{Smear} in units of radians/s), tracking rate (v_{Track} in units of radians/s), and integration time (t) previously introduced
- Optical PSF (PSF_{Optics}) characterized by the diffraction limit which is a function of the wavelength of light (λ), F/#, and detector pitch previously introduced as p
- Detector geometric and sampling PSFs ($PSF_{Detectors}$ and $PSF_{Sampling}$) characterized only by the detector pitch.

Equation 14:
$$S_{Image} = S_{Point} * PSF_{Atmosphere}(d_{SeeingDisc}) * PSF_{MotionBlur}(v_{Smear}, t, v_{Track}) *$$
$$PSF_{Optics}(p, F/\#,\ \lambda) * PSF_{Detectors}(p) * PSF_{Sampling}(p) \text{ [Electrons]}$$

For the purposes of a simple simulation, the atmospheric and optical PSF can be modeled as 2D symmetric Gaussian functions to represent their probabilistic distribution. The motion blur can be modeled as a 1D rectangle or 2D line function to represent the linear smearing effect and a 1D Gaussian function to represent to jitter that in this model is treated as a function of the tracking rate. Finally, the geometric detector and sampling or phase function PSFs can be modeled as 2D symmetric square functions to represent the geometric response of the detector and the uniform sampling probability function. An additional note is that the $PSF_{Detectors}$ should be peak normalized to unity to characterize the aggregation of signal by the detector, which could then be down-sampled with a comb function to produce a specific realization, or convolved with the $PSF_{Sampling}$ to get expected values that will be used for this analysis.

The 2D convolution is the first step that would require empirical simulation to this point. Although a closed form analytical solution may be achievable depending on the 2D PSFs involved for the purposes of rapid analytical

characterization, an evaluation was performed to compare the peak signal when generated empirically with the peak signal calculated analytically.

To calculate the analytical peak, a number of methods were attempted. However, best results were found by calculating the effective standard deviation of each PSF in two dimensions and RSS'ing each of the dimensional components together (Equation 15 and Equation 16). Next, calculating the two separate Gaussian equivalent peaks (Equation 17) and multiplying them together (Equation 18) can be completed as shown below to arrive empirically at a target signal peak (*S*) that is approximately equal to the analytical solution (Equation 19) and entirely avoids 2D convolution.

Equation 15: $\quad d_1 = \sqrt{Var_1(PSF_{Atmosphere}) + Var_1(PSF_{MotionBlur}) + Var_1(PSF_{Optics}) + Var_1(PSF_{Detectors}) + Var_1(PSF_{Sampling})}$ **[pixels]**

Equation 16: $\quad d_2 = \sqrt{Var_2(PSF_{Atmosphere}) + Var_2(PSF_{MotionBlur}) + Var_2(PSF_{Optics}) + Var_2(PSF_{Detectors}) + Var_2(PSF_{Sampling})}$ **[pixels]**

This can be slightly simplified if we orient the first dimension along the direction of motion blur, so that the variance of the motion blur along the second dimension is zero and the term drops out. Regardless, the peaks in each dimension can be calculated as shown in Equation 17 by integrating over a virtual center pixel and combined as in Equation 18 to provide a good analytical approximation of the peak of the discrete empirical simulation *S* in Equation 19.

Equation 17: $$peak_n = \int_{-1/2}^{1/2} \frac{1}{d_n\sqrt{2\pi}} e^{-\frac{x^2}{2d_n^2}} = \frac{1}{2}\left[erf\left(\frac{0.5}{d_n\sqrt{2}}\right) - erf\left(\frac{-0.5}{d_n\sqrt{2}}\right)\right] \text{ [ratio]}$$

Equation 18: $$PSF_{Peak} = peak_1\, peak_2 \text{ [ratio]}$$

Equation 19: $$S = Max(S_{Image}) \approx S_{Point}\, PSF_{Peak} \text{ [Electrons]}$$

To verify the accuracy of this analytical approximation, a range of empirical simulations were created to span the expected operational ranges (atmospheric PSFs from 0.25 to 2.0 pixels standard deviation in 0.25 pixel increments, optical PSFs from 0.25 to 2.0 pixels standard deviation in 0.25 pixel increments, and smear lengths from 0.0 to 20.0 pixels in length in 0.5 pixel increments), sorted by peak value, and the analytical approximation of the corresponding cases were plotted against them for comparison. The results are shown below in Figure 7 with an overall RMSE of only 0.0068 for the 2,624 test cases. The analysis performed for this evaluation was done in MATLAB, and for this suite of test cases, the time to empirically simulate the test targets 8x oversampled took 256 seconds total or about 97.7 milliseconds each, compared to analytically calculating the peak, which only took 0.15 seconds total or about 0.151 seconds total or about 57.6 nanoseconds, a speed increase of over 3 orders-of-magnitude. The actual implementation used for the MONET simulation was optimized from this in C++ to further increase the speed. From visual inspection and the low RMSE of these results, this process was considered excellent for this application and justified the use of this approach.

Now, with the full signal chain complete with a spatial PSF peak calculation, a fully analytic approach can be applied to both determine the sensor response of a target or conversely to calculate the target parameters given a detection criteria. For the MONET application, the two primary optical performance metrics are:

1. Minimum detectable target size
2. Necessary integration time to detect a target as a function of size

To achieve this first goal, the signal equations can be arranged to calculate the minimum detectable target size given a Signal-to-Noise (*SNR*) constraint. The *SNR* constraint could be acquired either by known operational detection algorithm performance or analytically derived as a probability of detection given either a known threshold or false alarm criteria. The *SNR* threshold can then be converted to a required signal if the background is known and both the signal and background can be treated as Poisson distributions, which is a good approximation for this detection scenario, and the definition of the SNR can be rewritten as in Equation 20 (where the target signal variance is identified as σ_{Signal}^2 and the background signal variance is identified as $\sigma_{Background}^2$). From there the definition can be rearranged to solve for S in terms of SNR and background shown in Equation 21.
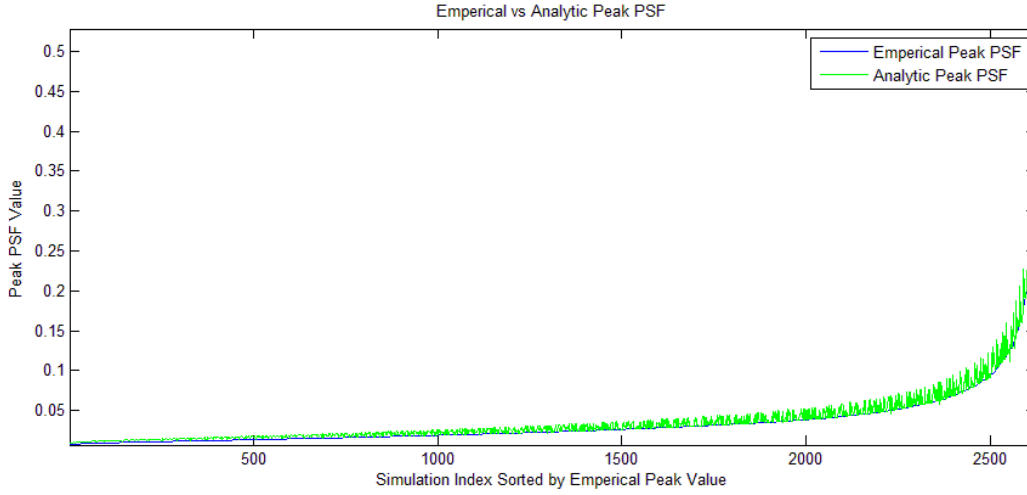
Figure 7. Plot of empirically simulated vs analytically calculated peak across operational range of parameters

Equation 20:
$$SNR = \frac{S}{\sqrt{\sigma_{Signal}^2 + \sigma_{Background}^2}} = \frac{S}{\sqrt{S+B}} \text{ [ratio]}$$

Equation 21:
$$S = \frac{SNR^2 + \sqrt{SNR^4 + 4SNR^2 B}}{2} \text{ [Electrons]}$$

Because target smear is a very large contributor to the target signal degradation, an alternative formulation of this can be done where a more advanced target detection algorithm is performed. A simple and linearly optimal detection method when a moderate amount of smear is present is using a matched filter, where if we create a linear matched filter to match the smear length of the target distribution then we can consider the *n*-samples where *n* is the number of smeared target pixels (equal to the smear rate in pixels per second multiplied by the integration time in seconds). This could give us a new matched filter SNR (SNR_MF) that is described in Equation 22, and again converted into an equivalent single-pixel or peak signal in Equation 23.

Equation 22:
$$SNR_{MF} = \frac{nS}{\sqrt{n\sigma_{Signal}^2 + n\sigma_{Background}^2}} \text{ [ratio]}$$

Equation 23:
$$S = \frac{nSNR_{MF}^2 + \sqrt{n^2 SNR_{MF}^4 + 4n^3 SNR_{MF}^2 B}}{2n^2} \text{ [ratio]}$$

This matched-filter approach is more reasonable given operational detection algorithms and for low target smear this will reduce to the previous definition in Equation 21. To address the first optical performance metric, we can solve for S from the given matched filter SNR threshold and smear rate, then put this in terms of the signal equations as in Equation 24 and then rearrange to solve for target size that will produce this signal value in Equation 25.

Equation 24:
$$S_{Peak} \approx \tau_{Atmosphere}(\theta) \frac{E_{Sun} S \rho \, Phase(\varphi) \, A_{Target}}{\pi \, d_{TargetToSensor}^2} A_{Aperture} \, \tau_{Optics} \frac{t \, SRF \, QE}{Q_\lambda} PSF_{Peak} \text{ [Electrons]}$$

Equation 25:
$$A_{Target} \approx \frac{S_{Peak} \pi \, d_{TargetToSensor}^2 \, Q_\lambda}{\tau_{Atmosphere}(\theta) \, E_{Sun} \, F \, \rho \, Phase(\varphi) A_{Aperture} \, \tau_{Optics} \, t \, SRF \, QE \, PSF_{Peak}} \text{ [m}^2\text{]}$$

A final step is to now represent this not as a signal value, but as a single pixel target signal rate (*s*) and single pixel background rate (*b*) that increase linearly with time. We can rearrange Equation 22 to replace *n* with $v_{Smear} t$, *S* with s/ v_{Smear} (because the single pixel target signal is inversely proportional to the smear rate), and *B* with *bt*. This gives

us Equation 26, which can then be rearranged to solve for integration time shown in Equation 27, addressing the second primary optical performance metric.

Equation 26:
$$\mathbf{SNR} = \frac{v_{Smear}ts/v_{Smear}}{\sqrt{v_{Smear}ts/r+v_{Smear}tbt}} = \frac{ts}{\sqrt{ts+v_{Smear}t^2b}} \text{ [ratio]}$$

Equation 27:
$$t = \frac{sSNR^2}{s^2-v_{Smear}bSNR^2} \text{ [s]}$$

6.2 <u>Probability of Cloud Cover Modeling for Optical Sensors</u>

Following the development of BSPACE weather modeling, we combine weather characterization accuracy α (incorporating both real-time assessment/status and forecasting, where 1 = perfect characterization) with Probability of Cloud Cover (P_{cc}=0 for perfectly clear hemisphere above a ground observing sensor) to assess the probability of attempting to collect the target (P_{look}) and the probability of actually seeing the target as follows (note that the inverse of P_{see} represents the statistical increase in optical collection resources needed to compensate for the effects of weather:

Equation 28:
$$\boldsymbol{P_{look}} = (\boldsymbol{\alpha})(\mathbf{1} - \boldsymbol{P_{cc}}) + (\mathbf{1} - \boldsymbol{\alpha})(\boldsymbol{P_{cc}})$$

Equation 29:
$$\boldsymbol{P_{see}} = (\boldsymbol{\alpha})\frac{(\mathbf{1}-\boldsymbol{P_{cc}})}{\boldsymbol{P_{look}}}$$

One could also incorporate the concept of weather persistence Wp over a target collection frequency F and we define maximum ground sensor satisfaction as shown in **Equation 30**, although for this paper we just chose to use $\boldsymbol{P_{look}}$ (above) to scale the cloud-free collection rate for a given sensor, and we ignored $\boldsymbol{P_{see}}$ and weather persistence under the assumption that cloud sensors onsite at the optical telescopes would be well-characterized and telescope housings would be responsive enough to make a lack of weather persistence a non-issue.

Equation 30:
$$\boldsymbol{Sensor\_Satisfaction} = \mathbf{1} - \boldsymbol{P_{cc}}^{F/Wp}$$

Probability of Cloud Cover (Pcc) and precipitation rate were evaluated over the years 2000 to 2014 by extensive statistical characterization of the global Reanalysis-2 data[2] as shown in Figure 8 and Figure 9. The median Pcc statistics are directly ingested into MONET as a function of month of year and global location, whereas the median annual precipitation rates could be incorporated into a radar or RF energy loss expression if so desired (but are not utilized by MONET at this time).
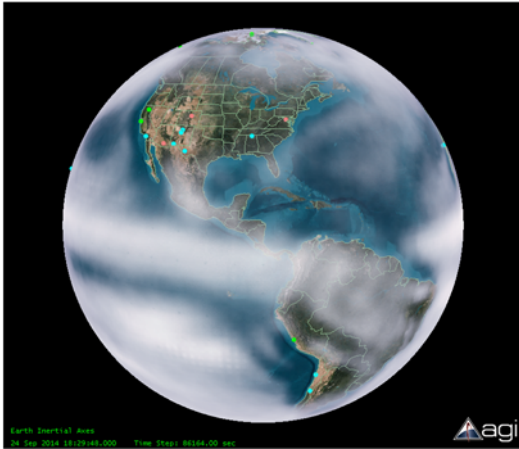

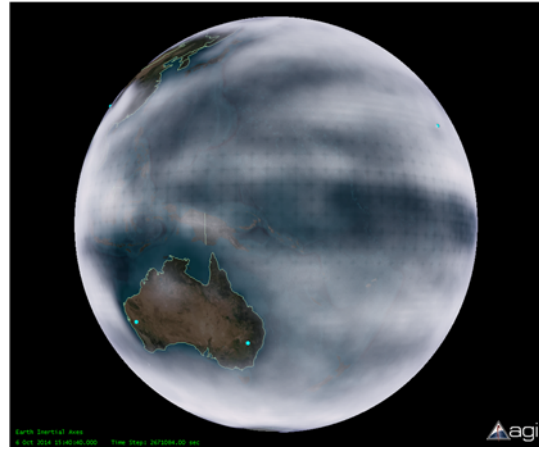Figure 8. Median monthly nighttime percent cloud cover aggregated over years 2000 to 2014 (western hemisphere).

Figure 9. Median monthly nighttime percent cloud cover aggregated over years 2000 to 2014 (EH).

6.3   Ground-Based Radar Sensor Modeling In MONET

For the purposes of initial radar sensor modeling in MONET, we consider the use of pulsed radars for the detection of LEO objects.   The two classes of radars considered are the Advanced Modular Incoherent Scatter Radar (AMISR) UHF phased array systems and dish-based radars. These are described in more detail below.

Radar Equation

The detection capability of a radar results from a combination of (a) the system parameters such as frequency / wavelength, transmit and receive gain, transmit power, system losses and system temperature (including noise figure), (b) target parameters such as range and cross-section, and (c) the integration time of the measurement. Our analysis begins with the radar equation, where the received power for a coherent point-like target (with physical dimensions much smaller than the illuminated volume) is given by,

Equation 31:
$$P_{rx} = \frac{P_{tx} G_{tx} G_{rx} \sigma \lambda^2}{(4\pi)^3 R_{rx}^2 R_{tx}^2 L}$$
(symbols defined in Table 1)

Table 1 Symbols, definitions, and units.

P_{rx}, P_n, P_{tx}	Received, noise, transmit power	Watts, W
G_{tx}, G_{rx}	Transmit, receive gain	
σ	Radar-scattering target cross-section	square-meters, m^2
λ	Radar wavelength	meters, m
k	Radar wavenumber	radians/meter, rad/m
R_{tx}, R_{rx}	Transmit and receive range to target	meters, m
L	Loss factor	
T_{sys}	System temperature	Kelvin, K
B	Receive bandwidth	Hertz, Hz
T_{int}	Integration time	Seconds, s
F	Duty Factor	
r, d	Target cross-sectional radius and diameter	meters, m

The noise power is related to the system temperature and receive bandwidth,

Equation 32:
$$P_n = \kappa_B T_{sys} B$$

where T_{sys} includes sky and system noise, with the dominant contributions to the latter being due to the noise figure of the low-noise amplifier at the antenna. The signal-to-noise ratio is then defined simply as,

Equation 33:
$$SNR = \frac{P_{rx}}{P_n}$$

Integration

Coherent integration can be used to boost target detectability. The amount of coherent detection possible is limited by the coherence of the target and the coherence of the radar, with the former being the main limitation for the levels of integration time considered here and using fully coherent radar systems.   Coherence requires amplitude stationarity (or accurate modeling of the amplitude coherence), and this is likely the main integration time limitation. Change in position within the radar beam must be accounted for in coherent detection.

Assuming a receive bandwidth matched to the transmit bandwidth, the increase in SNR from coherent integration over a time T_{int} is given by

Equation 34:
$$F\, T_{int}\, B$$

where *F* is the duty factor of the system. Turning the above equations around, we solve for the required integration time given a desired SNR level,

Equation 35:
$$T_{int} = SNR \frac{\kappa_B T_{sys}}{F P_{rx}}$$

Using the above equations for a fixed integration time and desired SNR level, we can solve for a minimum detectable cross-section.

Cross-section Model

For MONET, we require a model of radar-scattering cross-section to relate object size to object detectability. We utilize a simple approach of assuming metallic conducting spheres with diameter *d=2r*. Our simple radar cross-section consists of three regimes - the optical, Rayleigh, and Mie scattering regions - where the cross-sections are given by,

Equation 36:
$$\sigma_{optical} = \pi r^2$$

Equation 37:
$$\sigma_{rayleigh} = \sigma_{optical} \frac{64}{9} (\kappa r)^4$$

Equation 38:
$$\sigma_{mie} = \sigma_{optical} \left(1 \pm \sqrt{1.03(\kappa r)^{-5/2}}\right)^2, \kappa r > 1$$

Note that we do not attempt to model the detailed interference pattern in the Mie region, but the Mie cross-section defines the expected maximum and minimum cross section. For the region between the end of the Rayleigh regime and the start of the Mie region, we interpolate.

The cross-section normalized to the optical cross-section as a function of normalized radius (*kr*) is shown in Figure **10**. The cross-section drops as wavelength to the fourth power in the Rayleigh regime for fixed object radius. In the Mie regime, constructive and destructive may lead to enhanced or diminished scattering. In the optical regime, the object cross-sectional size determines the scattering cross-section.
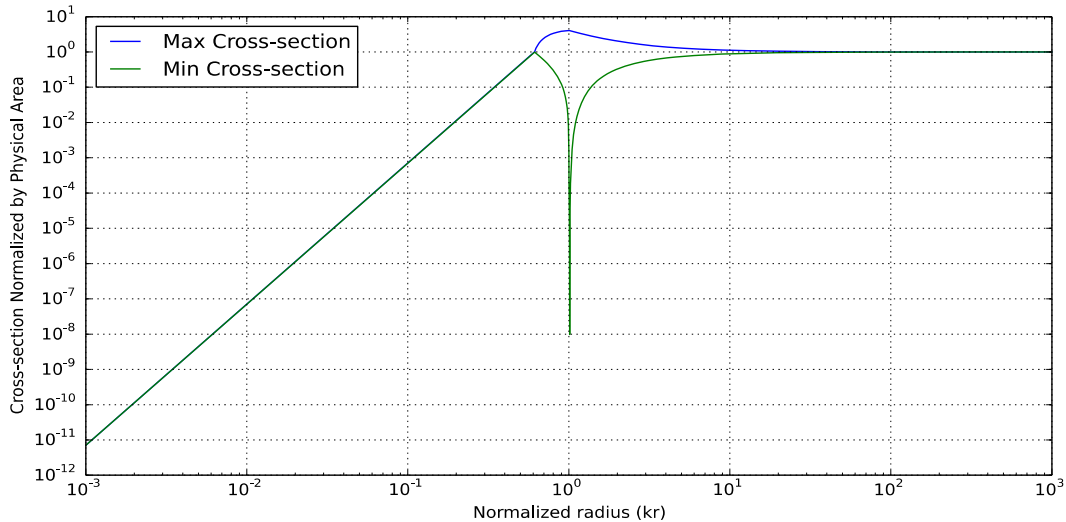

Figure 10. Normalized cross-section as a function of normalized radius for a metallic sphere.

This model can be used to move between radar scattering cross-section and object radius. For example, in Figure 11, we plot the cross-section as a function of object radius for three different probing wavelengths corresponding to a 3 GHz radar, a 1.290 GHz radar, and a 450 MHz radar. For detection of objects of a given size, a radar wavelength should be above the Rayleigh transition break point, i.e.

Equation 39:

$$\lambda \backsim > \left(\frac{64}{9}\right)^{1/4} 2\pi r$$

At 450 MHz, 1.290 GHz, and 3 GHz, these transitions occur at radii of approximately 6.5 cm, 2.2 cm, and 1 cm, respectively.
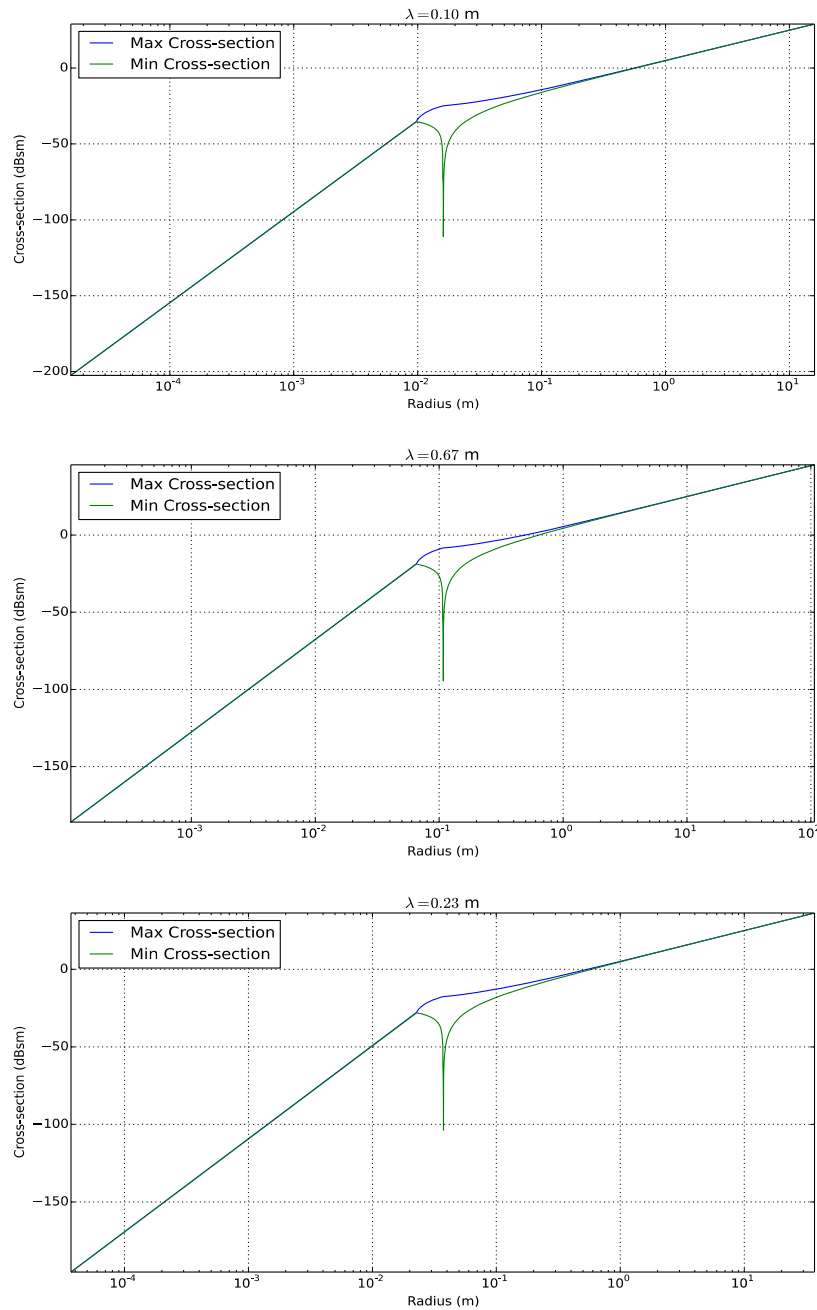

Figure 11. Cross-section in dBsm as a function of object radius for three different probing wavelengths.

Sensors

For the purposes of the initial MONET implementation, we consider the use of two classes of radar sensors: large phased array radar sensors and steerable dish-based radars. The technical specifications for these systems are listed in Table **2**.

Table 2 AMISR and Sondrestrom technical specifications.

Specification	AMISR (Full Face)	Sondrestrom
Peak Power	2 MW	3 MW
Max RF duty cycle	10%	3%
Pulse length	$1 - 2000~\mu s$	$1 - 500~\mu s$
Tx Frequency	430-450 MHz	1290 MHz
Antenna Gain	$\sim$43 dBi	49 dBi
Antenna Aperture	$\sim 715~m^2$	$\sim 800~m^2$
Beam Width	$\sim 1.1°$	$\sim 0.5°$
System Temperature	~ 120 K	~ 75 K
Steering	Pulse-to-pulse over $\sim \pm 25 - 35°$ from boresight (400 μs beamcode change time)	Elevation: $\sim > 10 - 20°$ depending o azimuth; Azimuth: $\pm 270°$ Scan rate: $\sim 5°/s$
Max Operations	Continuous, depending on power availability	Continuous, depending on power avai ability and onsite staffing availability
Other notable features	Unattended, fully remote operations	3-4 person on-site staff

AMISR Phased Array Radars

The Advanced Modular Incoherent Scatter Radar (AMISR) class of radar systems are modular, mobile radar facilities. The radars' main purposes are to perform studies of the upper atmosphere and ionosphere and to observe space weather events. SRI International, under a grant from the National Science Foundation (NSF), led the collaborative effort in the development of AMISR, whose novel modular configuration was designed to allow relative ease of relocation for studying upper atmospheric activity around the globe. Remote operation and electronic beam steering allow researchers operate and position the radar beam instantaneously to accurately measure rapidly changing space weather events.

Figure 12. PFISR (left) and RISR-N (right) systems.

AMISR now consists of three separate radar faces, with each face comprised of 128 building block-like panels over a ~32 by 28 meter surface. The first AMISR face was deployed in Poker Flat, Alaska in 2006 (the Poker Flat ISR, or PFISR), and the remaining two faces have been deployed in Resolute Bay, Nunavut, Canada (RISR-N and RISR-C), Figure 12. Future NSF AMISR deployments will be determined by a scientific advisory panel assembled at the behest of NSF.

An AMISR satellite and debris tracking capability has been developed, and these systems are now used routinely to track satellites. The system makes use of wide-bandwidth radar pulses and coherent processing to detect objects as small as 5-10 cm in size. Current satellite tracking at AMISR achieves a range resolution better than 20 meters.

Figure 13 shows range residuals using nearly 60,000 data points from hundreds of satellite passes over PFISR. Range residuals are approximately normally distributed over +/- 20 meters. Range biases have been shown to be stable with a standard deviation of less than 10 meters. The Doppler residuals are currently at the level of 75 cm/sec with coherent integration of 60 milliseconds.
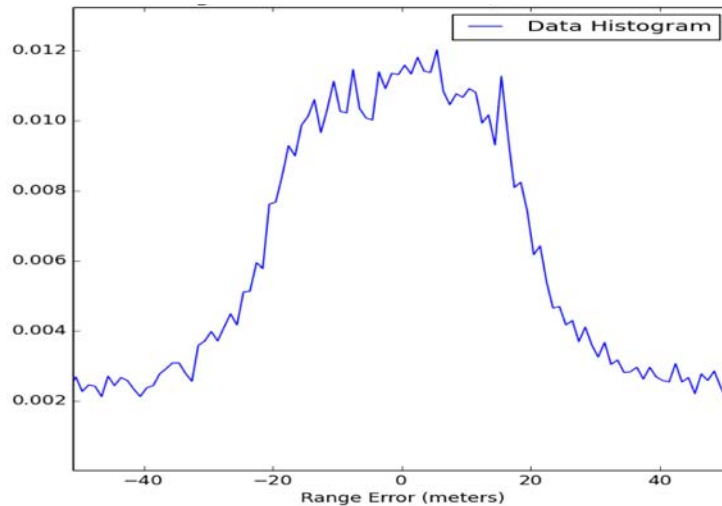

Figure 13. Range residuals using nearly 60,000 data points from satellite tracking with PFISR.

AMISR provides the measurement quality necessary for to create high-fidelity orbital solutions. This is demonstrated in Figure 14. PFISR tracked the LARETS satellite, whose position is precisely known from satellite laser ranging. The satellite is located in a polar orbit with an altitude of 685 km. Orbital solutions were computed with AGI's Orbit Determination Tool Kit (ODTK) from 15 passes of PFISR measurements, and compared against orbits fit to satellite laser ranging data. Figure 14 (top) shows that the measurement residuals are typically much less than 30 meters. Figure 14 (bottom) shows that the in-track difference between the two orbits is less than 30 meters and averages around 10 meters. Cross-track and range differences are even smaller. The in-track differences show one oscillation per orbit. The PFISR orbit was created with data from only one sensor, so this oscillation is an effect of under-sampling the orbit. However, PFISR takes enough measurements during each pass, and with a large angular separation, that the under-sampling oscillations are limited to less than 20 meters (peak to peak) over the entire orbit.

Sondrestrom Dish Radar

Just north of the Arctic Circle and 100 km inland from the west coast of Greenland, the Sondrestrom Upper Atmospheric Research Facility in Kangerlussuaq, Greenland is a research facility dedicated to studying the polar upper atmosphere.   The facility is operated by SRI International in Menlo Park, California, under the auspices of the NSF. The facility has been operating in Greenland since 1983.

This facility is host to more than 20 instruments, the majority of which provide unique and complementary information about the arctic upper atmosphere. Together, these instruments advance our knowledge of upper atmospheric physics and determine how the tenuous neutral gas interacts with the charged space plasma environment. The suite of instrumentation supports many disciplines of research, from plate tectonics to auroral physics and space weather. The facility instrumentation covers the electromagnetic spectrum while the data results span the spectrum of polar research.

The centerpiece instrument of the facility is an L-band incoherent scatter radar with a 32 meter fully steerable antenna. The IS radar technique is a powerful tool capable of measuring range-resolved ionospheric and atmospheric parameters simultaneously from the ground to the outer reaches of our atmosphere. Use of a steerable antenna allows spatial coverage in both latitude and longitude. See radar specifications in Table **2**.
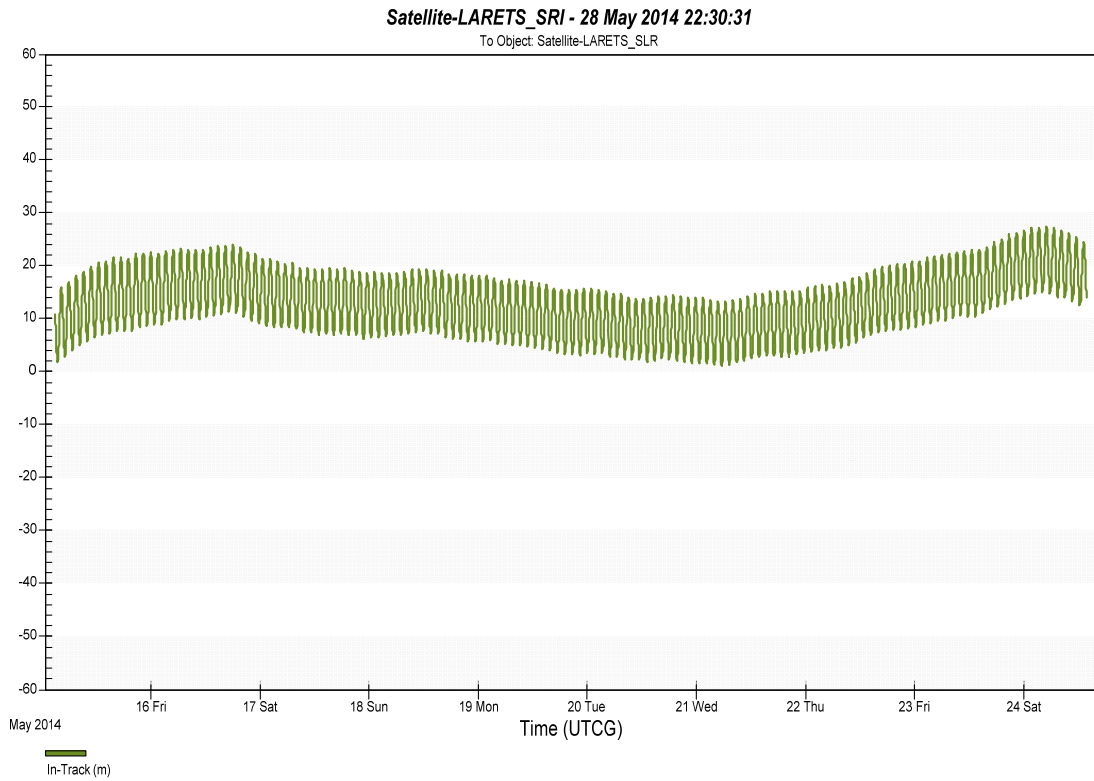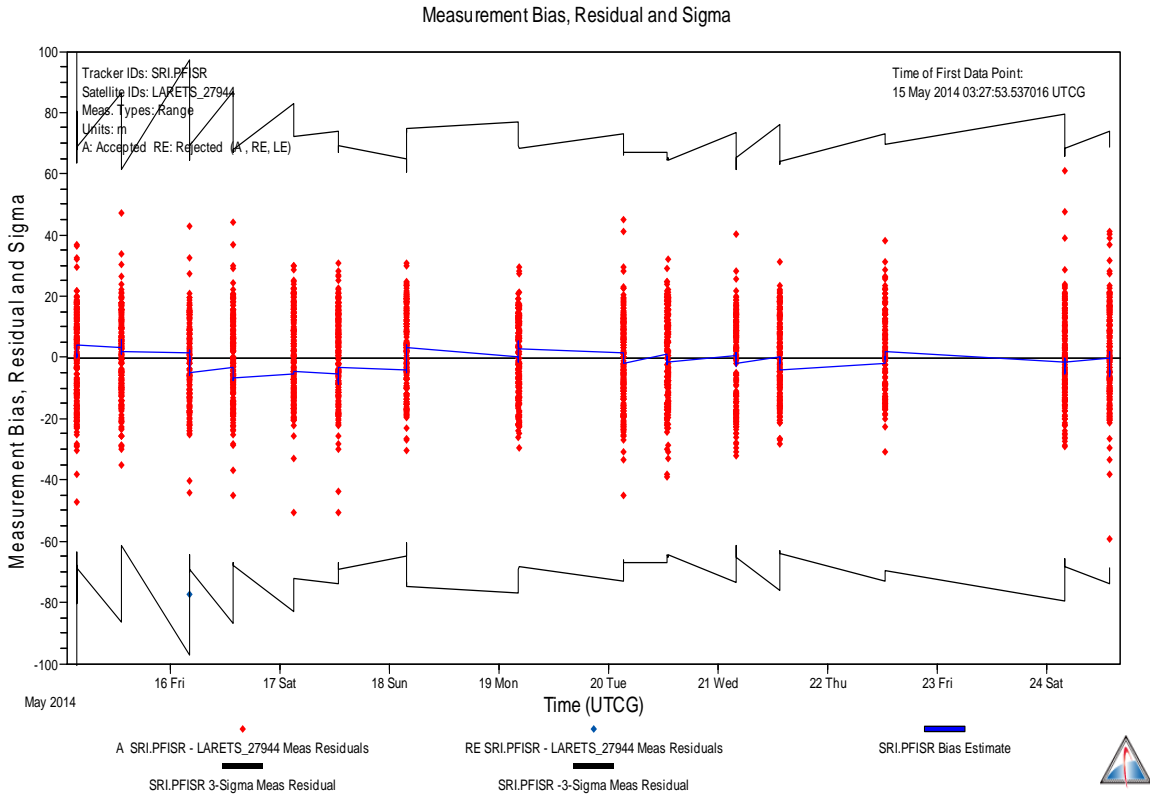
Measurement Bias, Residual and Sigma

Tracker IDs: SRI.PFISR
Satellite IDs: LARETS_27944
Meas. Types: Range
Units: m
A: Accepted RE: Rejected (A, RE, LE)

Time of First Data Point:
15 May 2014 03:27:53.537016 UTCG

Measurement Bias, Residual and Sigma

100
80
60
40
20
0
-20
-40
-60
-80
-100

May 2014   16 Fri   17 Sat   18 Sun   19 Mon   20 Tue   21 Wed   22 Thu   23 Fri   24 Sat

Time (UTCG)

A SRI.PFISR - LARETS_27944 Meas Residuals   RE SRI.PFISR - LARETS_27944 Meas Residuals   SRI.PFISR Bias Estimate

SRI.PFISR 3-Sigma Meas Residual   SRI.PFISR -3-Sigma Meas Residual

Satellite-LARETS_SRI - 28 May 2014 22:30:31
To Object: Satellite-LARETS_SLR

60
50
40
30
20
10
0
-10
-20
-30
-40
-50
-60

May 2014   16 Fri   17 Sat   18 Sun   19 Mon   20 Tue   21 Wed   22 Thu   23 Fri   24 Sat

Time (UTCG)

In-Track (m)

Figure 14.   (Top) Computed orbital solution residuals from PFISR measurements of 15 passes of the LARETS laser ranging satellite. (Bottom) In-track difference between orbits fit to PFISR data and vs. laser ranging data (y-axes units are meters).

Example: PFISR

Using the equations developed earlier in this section, we now explore the sensitivity of the PFISR system. Figure 15 shows the minimal detectable object size in dBsm as a function of range given an integration time of 100 milliseconds, a desired SNR of 10 dB, a system temperature of 300 K, and the maximum transmit power and radar duty cycle. At 1000 km, the radar can detect objects as small as ~ -40 dBsm. The lower panel of Figure 3.6 shows the corresponding object size using the cross-section model developed earlier. The spread of object sizes is a result of Mie scattering. For example, at a range of 1000 km it is predicted that the minimum detectable object size is in the range 5-20 cm. In turn, Figure 16 shows the required integration time to detect an object with a certain cross-section.
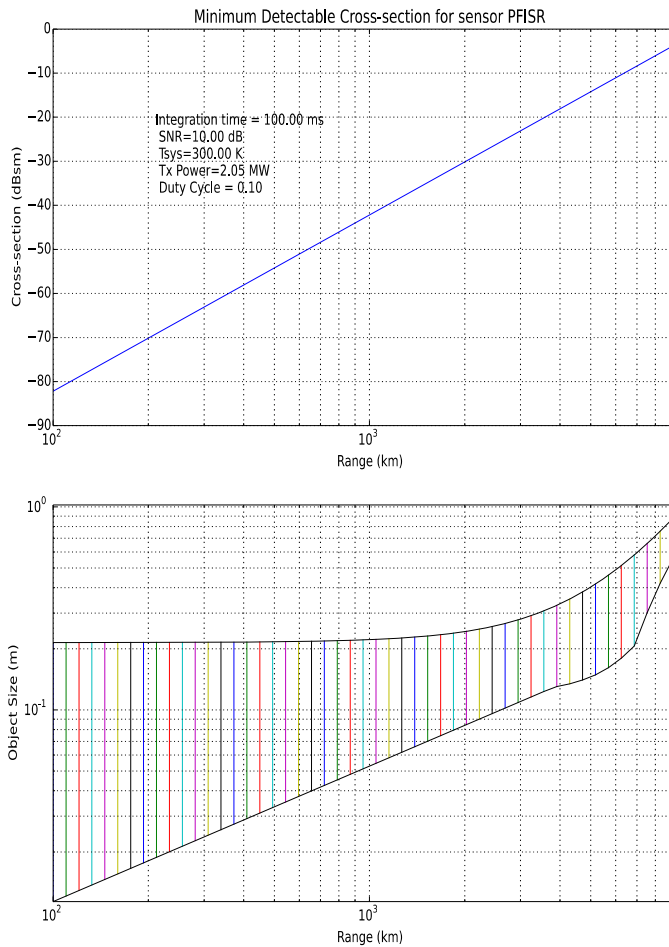
Figure 15. (Top) Minimum detectable cross-section and (bottom) corresponding object size range for PFISR.
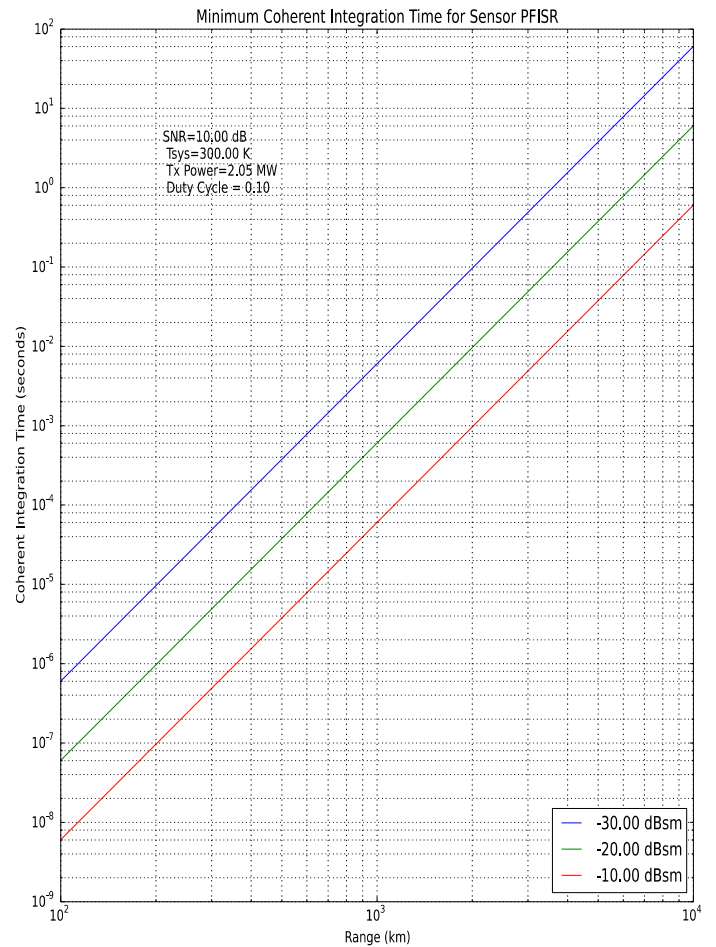
Figure 16. Minimum coherent integration time as a function of range for PFISR for three different scattering cross-sections.

A way to validate the methods described in this paper is to use objects of known size and estimate their cross-section from many measurements. We have done this analysis with PFISR for 4 spherical objects: Stella (24 cm), LARES (37.6 cm), LARETS (21 cm), and POPACS (10 cm). Each analysis consists of hundreds of passes, and the objects span different orbital altitudes in LEO. The histograms for each target are displayed graphically in Figure 17 and the median and mean values as compared to the predicted cross-sections are shown in Table **3**. Measurements for

all four targets fall within the predicted cross-section range. The objects span a predicted cross-section range of approximately 10-20 dB. Stella and LARETS are of similar size and the measured cross-sections are similar in magnitude. However, these targets are in the Mie regime where there is uncertainty about the expected cross-section. LARES, on the other hand, is a larger object, and its returns are comparatively larger. POPACS, the smallest objects analyzed, lie in the Rayleigh regime. The measured cross sections are within 2 dB of the predicted cross sections. Hence, we conclude that for the specific case when the target is actually a metallic sphere, consistent with our assumptions, the analysis leads to reasonable estimates of cross-section.

Table 3 Comparison of predicted and measured cross-sections for four targets.

Object	Predicted Cross Section	Measured Median Cross Section	Measured Mean Cross Section
LARES (37.6 cm)	-16 to -6 dBsm	-15.4 dBsm	-14.1 dBsm
Stella (24 cm)	-31.5 to -8.0 dBsm	-23.2 dBsm	-21.36 dBsm
LARETS (21 cm)	-32.6 to -8.5 dBsm	-26.8 dBsm	-24.6 dBsm
POPACS (10 cm)	-25.6 dBsm	-26.5 dBsm	-24.0 dBsm
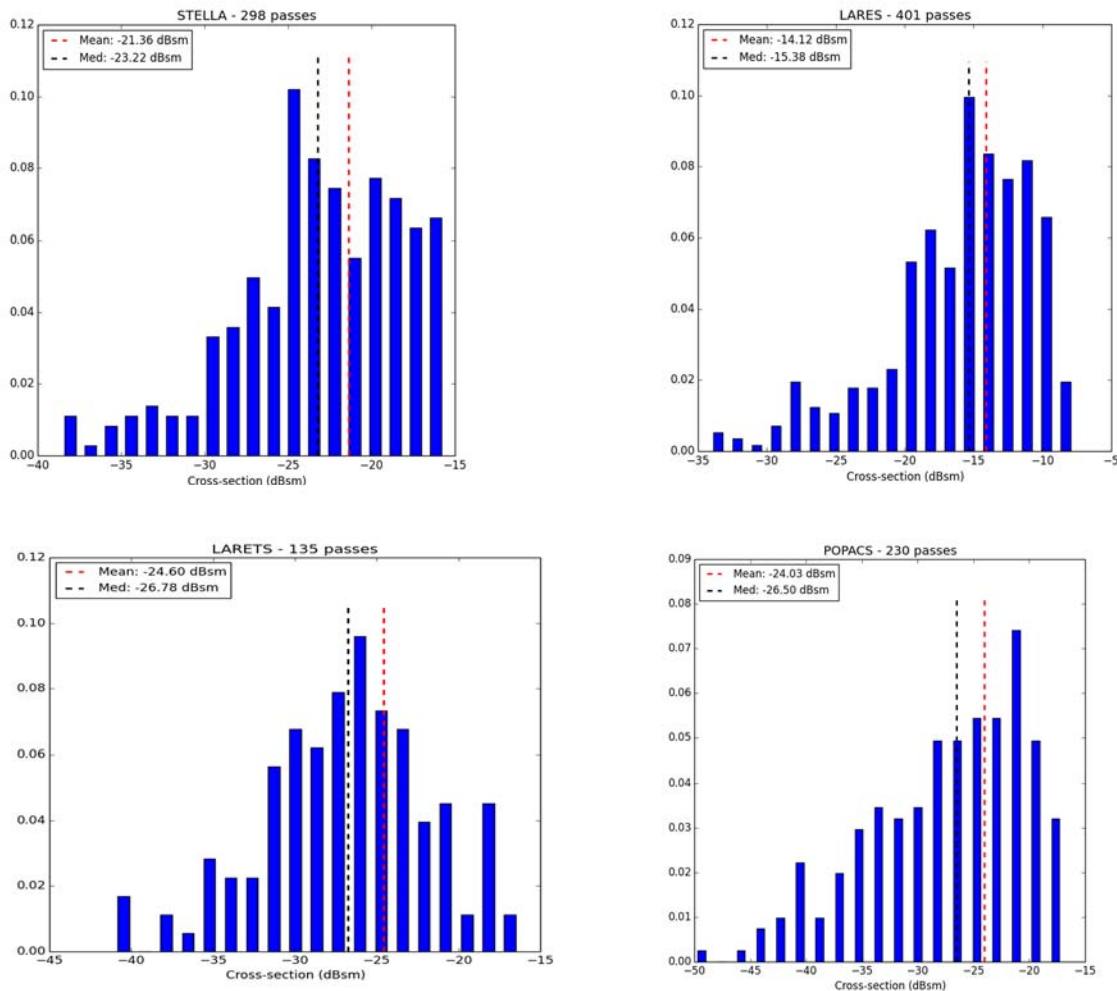
Figure 17. Cross-section histograms from hundreds of passes for (Top Left) Stella 24-cm sphere, (Top Right) Lares 37.6-cm sphere, (Bottom Left) LARETS 21-cm sphere, and (Bottom Right) POPACS 10-cm spheres. Black and red dashed lines show median and mean values of the distributions, respectively.

7. MOTIVATION: AGI'S NEW COMMERCIAL SPACE OPERATIONS CENTER (COMSPOC)

MONET was initially conceived to perform low-to-medium-fidelity system trades in the system concept development stage for Analytical Graphics Inc. (AGI's) new Commercial Space Operations Center[3] (ComSpOC) initiative. ComSpOC pairs up AGI's powerful SSA Software Suite with existing underutilized sensors, plus anticipated new sensors, to yield exquisite observation, association and tracking of Resident Space Objects (RSOs). ComSpOC's combination of cost-effective yet extremely capable optical, radar, passive RF sensors (Figure 18) provides a broad-spectrum, commercial alternative to achieving Space Situational Awareness.

One of AGI's goals for ComSpOC is to significantly increase the number of space objects being tracked. As depicted in Figure 19, the number of objects currently being tracked (left side, blue "bubbles" denote number of objects being tracked in the public catalog) is only three percent of the number of objects projected to be in space down to one centimeter in size (red bubbles on right).
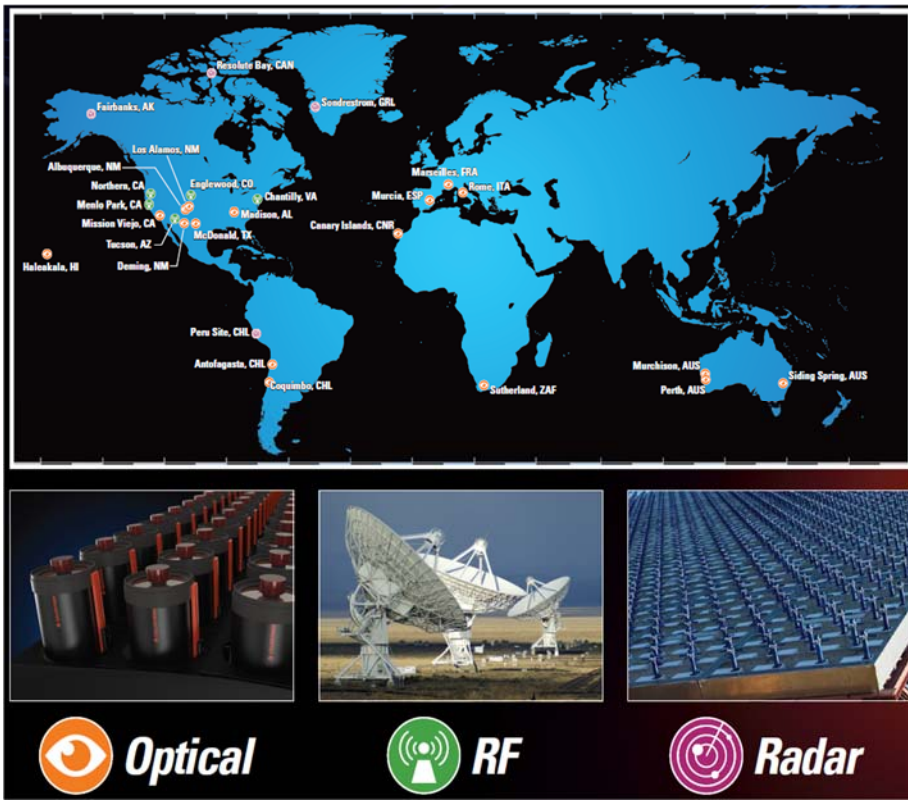
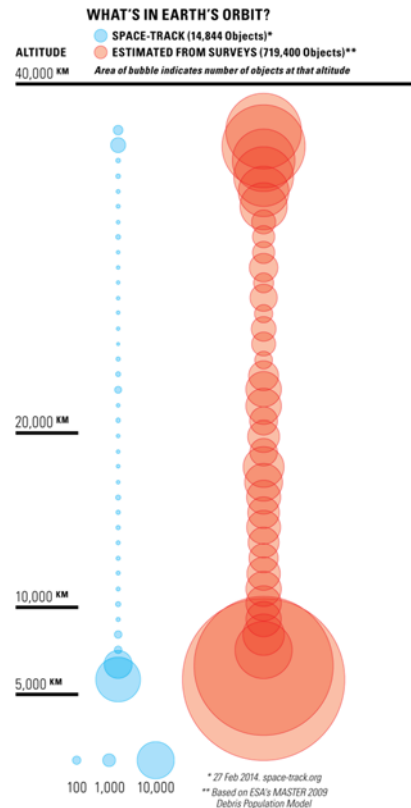Figure 18. Anticipated ComSpOC optical, passive RF and radar sensor sites.

Figure 19. Comparison of RSOs tracked in public catalog vs. estimated RSOs larger than 1 cm, by altitude.

8. MONET RESULTS AND CONCLUSIONS

To illustrate how MONET works, we will examine a purely hypothetical, but entirely achievable, notional sensor network comprised of optical and radar sensors attempting to track 150,000 space objects of sizes that are roughly in family with today's RSO catalog RCS values.

8.1 Sample Test Case

First, the observing network and the space population it is attempting to track must be defined.

The purely notional observing network architecture selected for illustrative purposes of this paper is summarized in Table 4.

Note that while we have not yet discussed passive RF sensors and are not including them in the example, such sensors could also be readily implemented in MONET, with passive RF rates of collection determined from average slew rates and dwell time and their ability to detect actively-transmitting (or reflecting) satellites based upon EIRP contours and antenna patterns.

Table 4 MONET Example optical (blue-hued) and radar (orange-hued) sensor laydown.

Sensor #	Sensor Description	Sensor Location	Sensors Avail	Apportionment per day (ea.)
1	0.4 m Optical Telescope	Australia, Eastern	1	1.0
2	1.0 m Optical Telescope	Australia, Eastern	1	0.2
3	2.0 m Optical Telescope	Australia, Eastern	1	0.05
4	0.4 m Optical Telescope	Chile	2	2.0
5	1.0 m Optical Telescope	Chile	1	0.2
6	0.5 m Optical Telescope	Italy	1	1.0
7	0.35 m Optical Telescope	Japan	1	1.0
8	0.2 m Optical Telescope (Kelso)	Maui	1	1.0
9	0.4 m Optical Telescope	Maui	1	1.0
10	2.0 m Optical Telescope	Maui	1	0.05
11	0.4 m Optical Telescope	South Africa	2	1.0
12	1.0 m Optical Telescope	South Africa	1	0.2
13	0.4 m Optical Telescope	Tenerife	1	1.0
14	PFISR	Alaska	1	0.5
15	RISR	Canada	1	0.5
16	Notional AMISR for smaller targets	Hawaii	1	1.0
17	Notional AMISR for smaller targets	California	1	1.0
18	Notional AMISR for smaller targets	Guam	1	1.0
19	Notional AMISR for smaller targets	Puerto Rico	1	1.0
20	Notional AMISR for smaller targets	Greenland	1	1.0

The optical and radar sensor coverage volumes associated with the above sensor laydown are shown in Figure 20 and Figure 21. The colors assigned to the volumetrics denote the smallest objects trackable at that viewing geometry and conditions. In Figure 20, magenta represents 1m objects and green represents 5m objects. In Figure 21, red thru yellow denotes 1 to 25 cm respectively and green thru blue denotes 1m objects respectively.

To model the space population (demand), SATCAT RCS values were adopted for radar cross-section as well as optical-facing surface area, with default values used whenever RCS values were unavailable[4]. Next, a public RSO catalog dated 29 June 2014 and consisting of 14923 RSOs was used. Note that in MONET, it is easy to utilize such a catalog to represent the tracking requirements associated with an inflated catalog (e.g. to represent 10 satellites by randomly drawing 10 in-track positions). Such an inflated space population is the set of requirements that we desire a space tracking network to be able to accommodate; a three-dimensional spatial density of the non-inflated public RSO catalog is portrayed in Figure 22 (LEO) and Figure 23 (GEO).
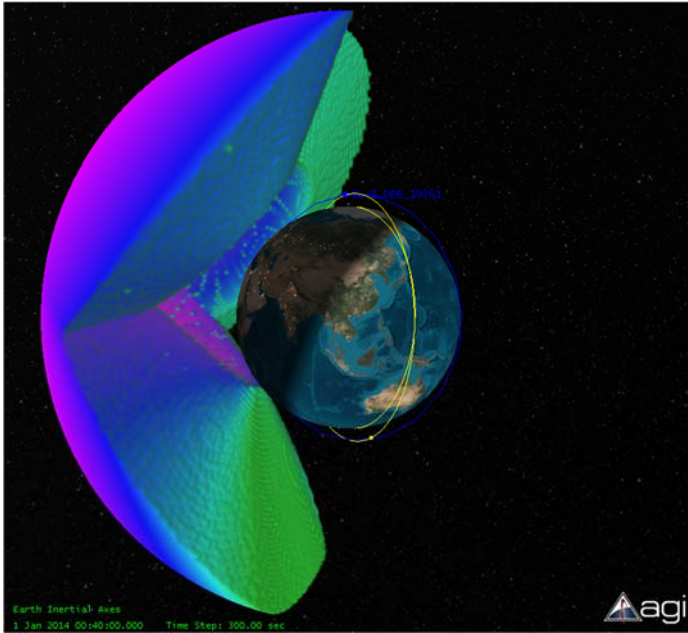
Figure 20. Optical sensor coverage volumes constrained up to 10,000 km altitude, color-coded by minimum-trackable object size w/magenta 1 m and green 5 m
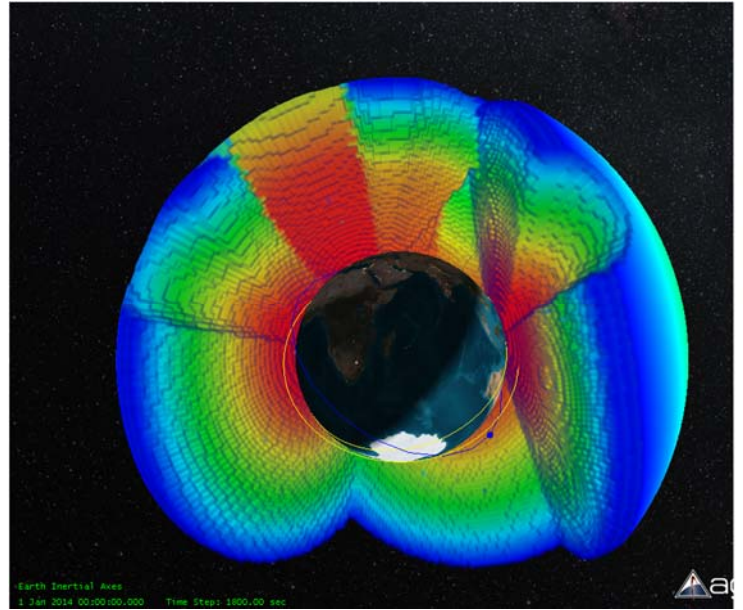

Figure 21. Radar sensor coverage volumes constrained up to 10,000 km altitude, color-coded by minimum-trackable object size with red 1 to 10 cm and green/blue up to 1 m.
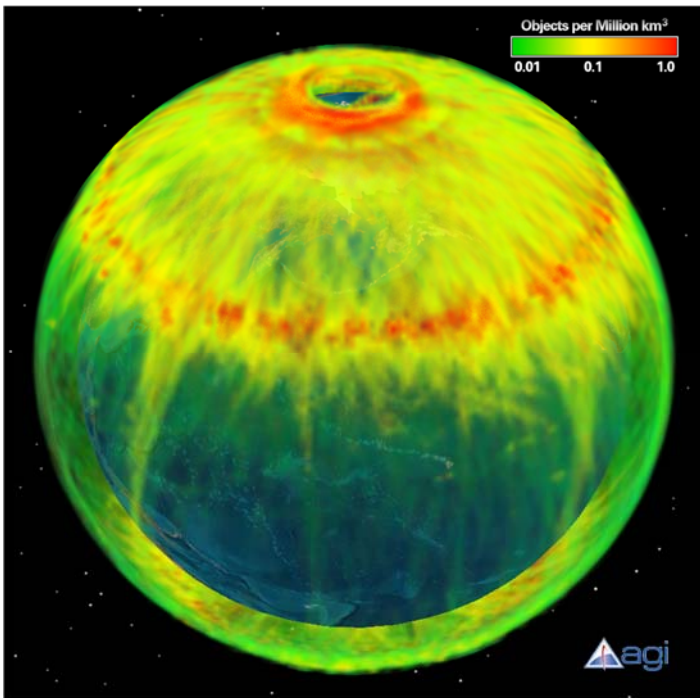

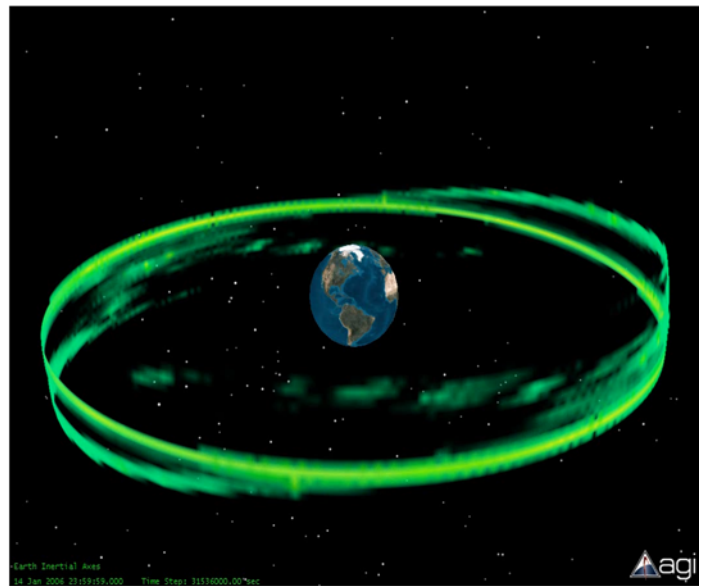Figure 22. Spatial density of the LEO regime up to 1000 km.

Figure 23. Spatial density of the GEO regime ± 2000 km.

8.2   MONET Results for the Sample Test Case

MONET analyzed the above test case. MONET can provide wealth of sensor metrics and approaches to portray the performance of the system-of-systems sensor network, to include probability density function (PDF) characterizations, performance by sensor and sensor type, percent satisfaction by space object, crude estimates of orbit determination resultant accuracy (when a suitable OD heuristic is incorporated). Summary results for the optical sensors in our notional example test case are provided in Figure 24 and Figure 25. Results for the radars of the sample test case are shown in Figure 26 and Figure 27.
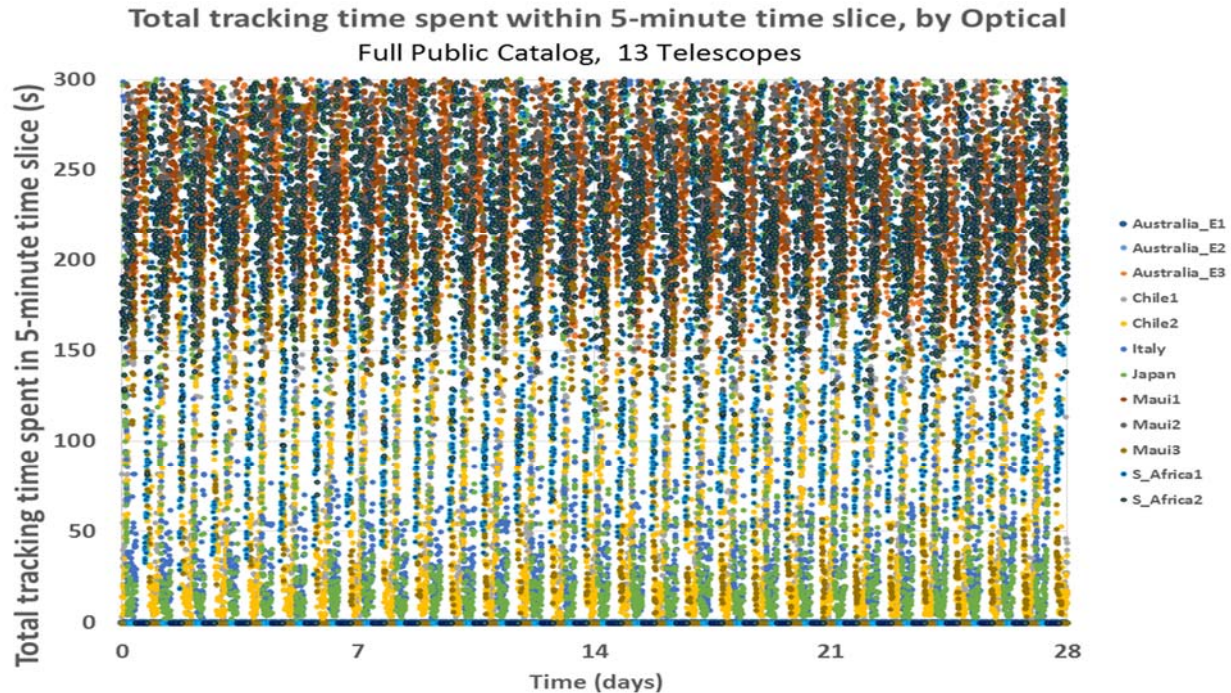
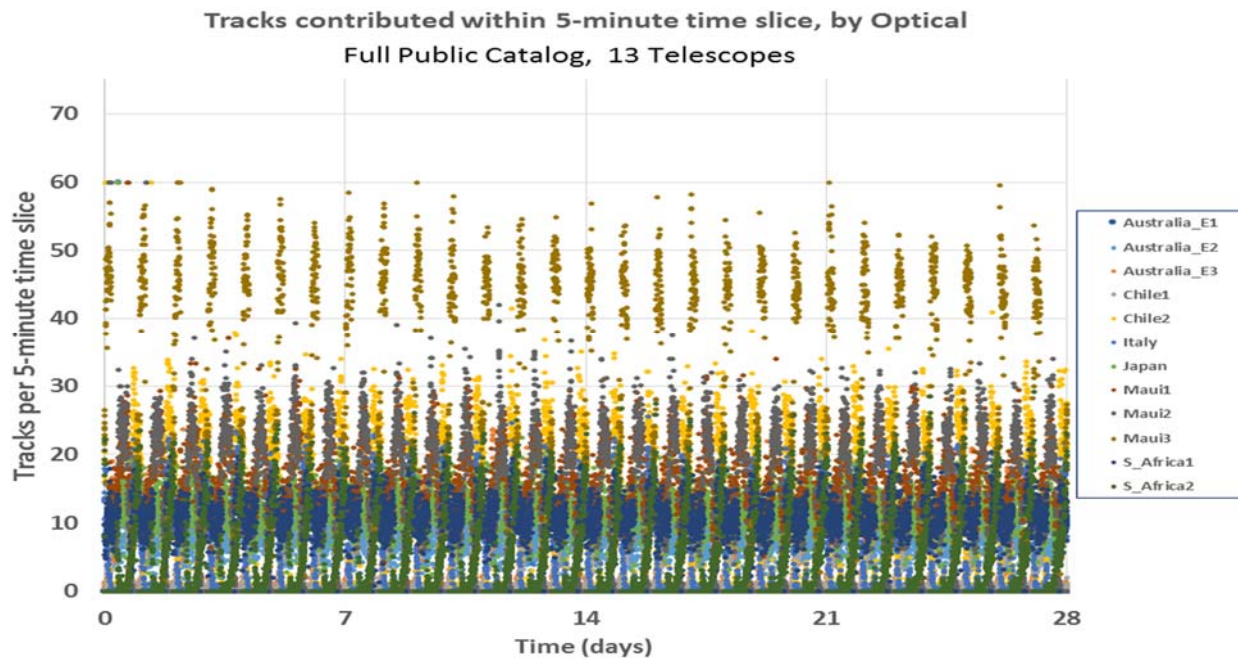Figure 24. Total radar tracking time spent by each sensor within each 5-minute tracking slice

Figure 25. Total radar tracks accomplished by each sensor within each 5-minute tracking slice
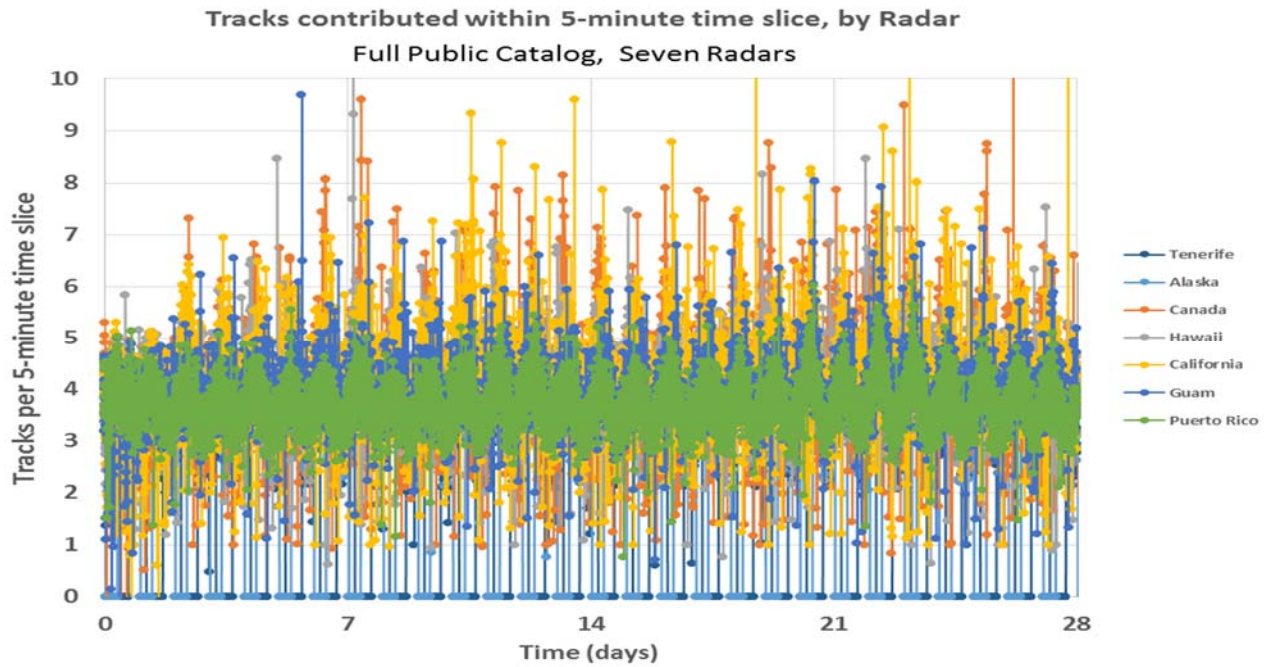
Figure 26. Total optical tracking time spent by each sensor within each 5-minute tracking slice
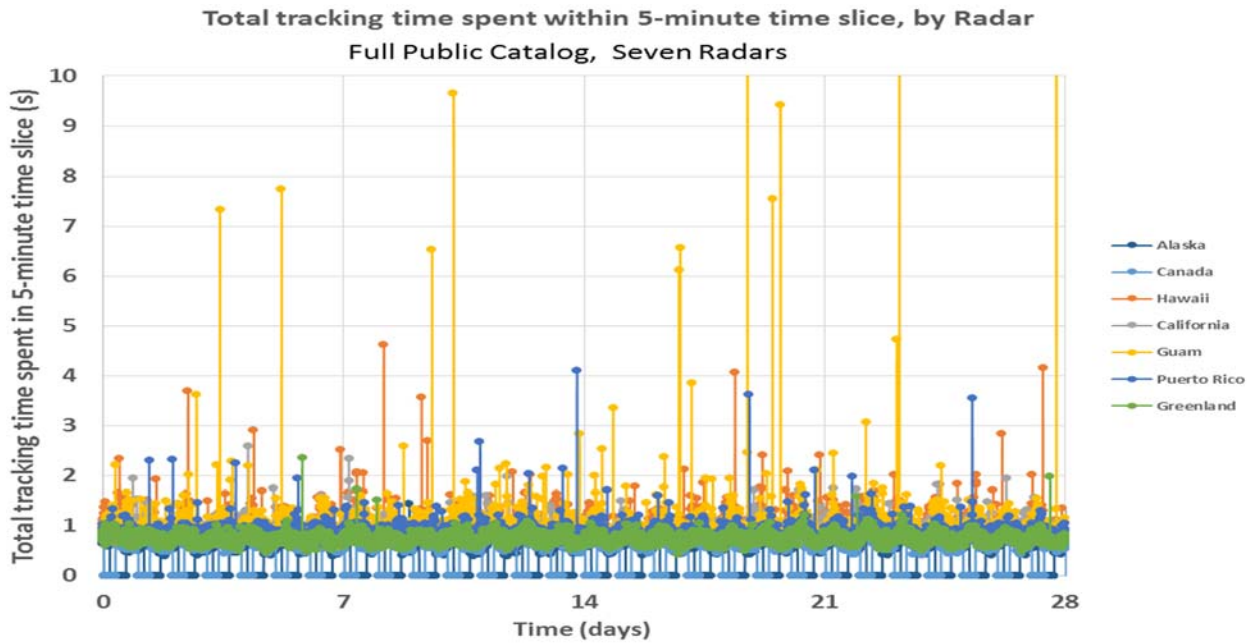

Figure 27. Total optical tracks accomplished by each sensor within each 5-minute tracking slice

Figure 24 and Figure 25 show the lighting-driven cyclical nature of optical sensor supply time loading. For GEO objects, the optical sensors with large coverage volumes of RSOs with slow angular rates perform the bulk of tracking, whereas in LEO objects, the radar's all-weather tracking coupled with extremely high track rates make it the dominant contributor.

9. Conclusions

The utility and capabilities of the Multi-phenomenology Observations Network Evaluation Tool (MONET) have been presented. This approach uses digitization coupled with medium-fidelity optics and radar models give credence to the methodology.

10. Future Work

There are many topics for future work associated with MONET:
- As coded, MONET runs 20 sensors against the full catalog for one month in several hours on an i7 simple laptop. While not too bad, we have already identified and are implementing ways to speed up processing further.
- MONET is also well-suited for a parent GA calling function.
- As sensor tracking rates are sometimes limited by network bandwidth to/from the site, we may explore a second digitized supply to model the network and buffer queues and bandwidth.
- IR and laser illumination are a top priority on the sensor modeling side.
- Conceiving and implementing of sensor cost-vs-performance metrics
- Creation and analysis of large-scope pace population catalogs based on best-of-breed space population models, including 150,000 (down to 2 cm) and 720,000 (down to 1 cm) catalogs
- Model passive RF sensor networks
- Develop and implement improved resultant OD heuristics and accuracy analyses
- Create additional MONET results metrics and graphs
- Run MONET to assess percent satisfaction of tracking RSOs, and then create spatial density plots of the objects with unsatisfactory performance (e.g. < 50% each day).

11. Acknowledgements

12. References

[1] Hayes, E.W., Hopkins, R., Hast, S., Karrenberg, H., Miyamoto, J.Y., Lang, T. and Oltrogge, D., "The BSpace Algorithm: A Statistical Model of Satellite Constellation Performance," AIAA Astrodynamics Specialist Conference, August 2004.

[2] NCEP_Reanalysis 2 data provided by the NOAA/OAR/ESRL PSD, Boulder, Colorado, USA, from their Web site at http://www.esrl.noaa.gov/psd/.

[3] Houlton, B. and Oltrogge, D., "Commercial Space Operations Center (ComSpOC): A Commercial Alternative for Space Situational Awareness (SSA), 2014 Space Symposium, Colorado Springs, 21 May 2014.

[4] Peterson, G.E., "Determining Object Sizes from Radar Cross Section for Collision Avoidance," AAS 05-307.